J Adv Ceram

Research Article

Reactive-precursor-assisted low-temperature densification of high-entropy (TiVNbTaMo)C_x ceramics with tunable mechanical and tribological properties

Jingwen Song[1], Mingliang Li[1,2,3], Hailong Wang[1,2,3,✉], Pengbo Zhao[4], Ziqi Zhao[1], Wei Li[1,✉], Kehao Zhang[1,2,3], Kai Zhang[1], Rui Zhang[1]

Cite this article: Song J, Li M, Wang H, et al. *J Adv Ceram* 2026, **15**(3): 9221242. https://doi.org/10.26599/JAC.2026.9221242

ABSTRACT: The preparation of dense high-entropy carbide ceramics (HECCs) is extremely challenging owing to their strong covalent bonding and sluggish diffusion associated with high-entropy effects, which necessitate ultrahigh sintering temperatures that in turn cause severe grain coarsening and excessive energy consumption. In this study, a novel low-temperature consolidation route is developed based on Ti_3AlC_2 reactive sintering. Specifically, the reactive precursor Ti_3AlC_2 decomposes into TiC_x and Al during spark plasma sintering. The *in situ* formed TiC_x accelerates interdiffusion and solid-solution formation among transition-metal carbides, while the released Al effectively activates particle interfaces. This dual-activation mechanism markedly enhances sintering kinetics, enabling the densification of (TiVNbTaMo)C_x ceramics at 1550 °C. The optimized sample achieved a relative density of 98.5%, a Vickers hardness of 22.94 GPa under a load of 9.8 N, a flexural strength of 1018 MPa, and a fracture toughness of 5.67 MPa·$m^{1/2}$, showing superior strength and hardness compared with most reported high-entropy carbides while maintaining an acceptable level of toughness. Furthermore, the interfacial modification results in a stable friction coefficient from room temperature to 900 °C, accompanied by nonadhesive wear behavior at elevated temperatures, making the obtained samples promising for high-temperature structural and wear-resistant applications. Therefore, reactive-Ti_3AlC_2 precursor-assisted sintering provides a new pathway for the design and scalable fabrication of advanced dense high-entropy ceramics under low-temperature conditions.

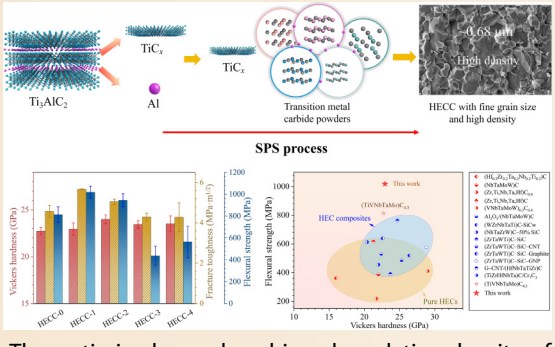

KEYWORDS: high-entropy carbide ceramics (HECCs); Ti_3AlC_2; *in situ* reaction; low-temperature densification; mechanical properties; tribological behavior

1 Introduction

High-entropy carbide ceramics (HECCs) have attracted growing attention owing to their outstanding hardness, good resistance to oxidation, corrosion, and tribological degradation [1]. These exceptional properties render HECCs promising candidates for high-temperature structural applications, including thermal insulation in spacecraft and gas turbines, cutting tools, and ultrahigh-temperature coatings in nuclear reactors and jet engines [2,3]. However, the strong covalent bonding and high-entropy effects that strengthen HECCs also inhibit atomic diffusion and grain boundary migration, making the densification of HECCs a formidable challenge [4].

As is well known, a high degree of densification is essential for achieving superior mechanical properties in ceramics [5]. For high-entropy carbides, a high temperature of approximately 2000 °C is required to achieve high densification, yet such elevated temperatures can accelerate grain growth, thereby impairing the mechanical performance of the ceramics [6–8]. Considerable efforts have been devoted to promoting densification through various approaches [9–15]. Among these strategies, optimization of the starting materials and the incorporation of sintering aids have proven effective in promoting the densification of HECCs at relatively low temperatures. Raw powders with fine grain sizes or optimized surface states exhibit enhanced sintering driving forces due to the reduction in total interfacial and surface energies,

[1] School of Materials Science and Engineering, Zhengzhou University, Zhengzhou 450001, China. [2] Zhongyuan Critical Metals Laboratory, Zhengzhou University, Zhengzhou 450001, China. [3] National Key Laboratory of Special Rare Metal Materials, Zhengzhou University, Zhengzhou 450001, China. [4] School of Materials Science and Engineering, Luoyang Institute of Science and Technology, Luoyang 471023, China.

✉ Corresponding authors. E-mail: W. Li, liw@zzu.edu.cn; H. Wang, 119whl@zzu.edu.cn

Received: November 6, 2025; Revised: December 17, 2025; Accepted: January 5, 2026

thereby accelerating atomic diffusion and facilitating neck formation between particles [16,17]. Nevertheless, the high reactivity and susceptibility to oxidation, agglomeration, and poor storage stability of such fine powders, together with the costly synthesis and handling, severely limit large-scale applications. Sintering aids function by enhancing atomic diffusion and activating solid-solution or liquid-phase sintering, thereby promoting pore elimination [18–24]. Anwer *et al.* [22] achieved nearly full densification of (Ti,V,Nb,Ta,W)C with the addition of 12 vol% Ni at 1420 °C, but the resulting composite exhibited moderate hardness (~14.3 GPa) due to the presence of the ductile Ni addition. Alternatively, metallic elements capable of forming solid solutions within the carbide lattice, such as Cr and Zr, have been introduced to facilitate densification through accelerated atomic diffusion and lattice distortion, thereby avoiding strength degradation [18,20,21]. However, the limited solid solubility of Cr and Zr restricts their applicability, therefore revealing the necessity for a generalizable low-temperature route capable of achieving densification while maintaining mechanical robustness.

Reactive sintering is an efficient approach to achieve densification by utilizing *in situ* chemical reactions to form target phases while enhancing mass transport. Among various systems, Ti_3AlC_2, a representative MAX-phase compound, has shown great potential as both a reactive precursor and sintering aid, owing to its ability to decompose into TiC_x and Al-containing species at elevated temperatures [25,26]. Ji *et al.* [27] employed Ti_3AlC_2 as an additive to fabricate high-entropy diboride ceramics via spark plasma sintering. The *in situ* decomposition of Ti_3AlC_2 not only promoted reactive sintering and solid-solution formation but also induced the formation of high-entropy carbide nanoparticles, thereby contributing to the remarkable enhancement of mechanical properties.

In this study, the influence of *in situ* TiC_x formation and Al-induced activation on the densification and mechanical properties of high-entropy (TiVNbTaMo)C_x ceramics was systematically investigated. In addition, the reaction-associated surface evolution and its influence on the high-temperature tribological behavior were also evaluated. This reactive *in situ* sintering strategy offers a broadly applicable pathway for achieving low-temperature densification of high-entropy carbide ceramics while maintaining good mechanical and tribological properties.

2 Materials and method

2.1 Synthesis of (TiVNbTaMo)C_x high-entropy ceramics

Initial powders Ti_3AlC_2, TiC, VC, NbC, TaC, and Mo_2C with average particle sizes of 1–3 μm and 99% purity were purchased from Beijing HwrkChemical Technology Co., Ltd. The molar ratio of Ti, V, Nb, Ta, and Mo in the starting materials was set as 1 : 1 : 1 : 1 : 1. The molar ratios of the starting materials for samples HECC-0 to HECC-4 are listed in Table 1. The powders were mixed in a polytetrafluoroethylene (PTFE) jar using a planetary ball mill at a speed of 300 r/min for 480 min. Tungsten carbide balls were employed as the milling media, with a ball-to-powder mass ratio of 10 : 1. Ethanol was applied as the milling medium. The mixed powders were obtained by drying the slurry using a rotary evaporator. The dried powders were then loaded into a graphite die and consolidated under vacuum via spark plasma sintering (SPS) at 1550 °C for 15 min under a uniaxial pressure of 50 MPa.

2.2 Characterizations

X-ray diffraction (XRD) data were collected using an Empyrean diffractometer (PANalytical, the Netherlands) equipped with a Cu Kα radiation source (λ = 1.5406 Å) for phase identification and analysis. The bulk density of the obtained samples was measured by the Archimedes method. The relative density was evaluated by comparing the experimental value with the theoretical density, which was calculated based on the lattice parameters obtained from XRD refinement. Thermogravimetry-differential scanning calorimetry (TG-DSC) analysis was carried out on a TGA/DSC 3+ system (METTLER TOLEDO, Switzerland). The tests were performed in a flowing argon atmosphere with a heating rate of 30 °C min^{-1} in the temperature range of 30–1500 °C. The surface and fracture morphologies were investigated with a field-emission scanning electron microscope (Sigma 300, ZEISS, Germany) coupled with an energy-dispersive X-ray spectroscope (EDS). The grain size of the ceramics was statistically evaluated from the fracture surface morphologies. Further analysis of selected regions was conducted using a JEM-F200 instrument (JEOL, Japan), which provided high-resolution TEM images, SAED patterns, and EDS mappings for detailed characterization of the lattice structure, phase composition, and elemental distribution. An X-ray photoelectron spectroscope (K-Alpha, Thermo Fisher, USA) was employed to analyze the bonding characteristics. To eliminate surface contamination, samples were etched with Ar ions before measurement. The binding energy step size was set to 0.1 eV. Both survey spectra and high-resolution spectra of C 1s, Ti 2p, V 2p, Nb 3d, Ta 4f, and Mo 3d were recorded.

The flexural strength was measured using a three-point bending test in accordance with ISO 6872:2015, employing bar-shaped specimens with dimensions of 16 mm × 3 mm × 2 mm and a 10 mm support span, and calculated following the standard procedure. The fracture toughness was evaluated using the single-edge notched beam (SENB) method in accordance with ASTM E1820. Specimens with dimensions of 22 mm × 4 mm × 2 mm were prepared, and a 2 mm precrack was introduced following the standard prenotching procedure. The support span was set at 16 mm, consistent with the referenced configuration, and the loading rate was 0.05 mm/min. All tests were conducted under ambient conditions. Vickers hardness was measured using a digital microhardness tester (HXD-1000TMC/LCD, Shanghai Taiming Optical Instrument Co., Ltd., China) under loads ranging from 0.49 to 9.8 N, with dwell time of 15 s. Each sample was indented at least 15 times at different positions to ensure statistical reliability. Crack propagation around indentations under a load of 9.8 N was further observed by SEM. The relationship between the

Table 1 Molar ratios of the starting materials for the HECC-0 to HECC-4 samples

	Ti_3AlC_2	TiC	VC	NbC	TaC	Mo_2C
HECC-0	0.000	1.00	1	1	1	0.5
HECC-1	0.017	0.95	1	1	1	0.5
HECC-2	0.033	0.90	1	1	1	0.5
HECC-3	0.050	0.85	1	1	1	0.5
HECC-4	0.067	0.80	1	1	1	0.5

mechanical properties and grain size was further analyzed using the Hall–Petch-type equations in Eq. (1):

$$H = H_0 + k \cdot d^{-1/2} \quad (1)$$

where H is the Vickers hardness, H_0 is the intrinsic hardness of the matrix, k is the Hall–Petch constant related to grain-boundary strengthening, and d is the average grain size.

The tribological properties were evaluated using a rotational tribometer (HT-1000, Lanzhou Zhongke Kaihua Technology Development Co., Ltd., China) under vacuum conditions. Si_3N_4 balls with a diameter of 6 mm were employed as the tribo-pairs. Each test was conducted for 30 min under an applied load of 9.8 N with a wear track radius of 5 mm, corresponding to a total sliding distance of 200 m. The friction coefficient was continuously monitored throughout the tests. The volumetric wear rate (W) was calculated as $W = V/(FL)$, where V is the volume loss, F is the applied load, and L is the sliding distance.

The wear volume of the samples was determined using a stylus profilometer. The three-dimensional (3D) surface morphologies of the wear tracks were obtained using a laser confocal microscope (S neox 090, Sensofar, Spain). All measurements were repeated three times to ensure reproducibility.

3 Results and discussion

3.1 Phase composition

The TG-DSC curves of the mixed powders (Fig. S1 in the Electronic Supplementary Material (ESM)) reveal distinct thermal behaviors between HECC-0 and HECC-4 under an Ar atmosphere. HECC-0 shows a small weight increase of approximately 0.7% up to 1500 °C. In contrast, HECC-1 exhibits a gradual weight loss with increasing temperature, totaling 4.8% at 1500 °C. A noticeable weight loss accompanied by an endothermic peak occurs at 1323 °C, consistent with the reported decomposition of Ti_3AlC_2 [28]. Therefore, the sintering temperature should be set above 1323 °C. These features probably arise from Al-assisted surface modification and transient phase evolution, reflecting the modified interfacial chemistry, consistent with thermodynamic predictions from the Ellingham diagram [29]. The sintering curves of HECC-0 and HECC-1 are illustrated in Fig. S2 in the ESM. Interestingly, the displacement curve of HECC-0 exhibits a short plateau at approximately 1520 °C, while HECC-1 exhibits a sharp inflection instead of a plateau, and the shrinkage resumes rapidly thereafter, indicating the rapid densification rate in HECC-1 samples.

The XRD patterns of HECC 0–4 are presented in Fig. 1(a). All samples exhibit diffraction peaks that can be indexed to a single rock-salt structure with the space group $Fm\bar{3}m$ (No. 225), indicating the formation of a simple face-centered cubic (fcc) solid solution. All diffraction peaks are well indexed to a single high-entropy carbide structure, without any secondary phases, including TiC_x and Al-related compounds [25]. When the Ti_3AlC_2 : TiC ratio exceeds 16.67 : 60, the single-phase structure can no longer be maintained. To further verify the phase composition and microstructural characteristics of the (TiVNbTaMo)C_x high-entropy ceramics, transmission electron microscopy (TEM) analyses were conducted. The selected-area electron diffraction (SAED) pattern (Fig. 2(b) in the ESM), taken along the [$\bar{1}$00] zone axis, exhibits sharp diffraction spots corresponding to a single FCC structure, consistent with the XRD results (Fig. 1(a)). Figure 2(c) shows a representative high-resolution TEM (HRTEM) image, where clear lattice fringes with an interplanar spacing of approximately 0.22 nm can be observed, corresponding to the (002) plane. Moreover, the measured lattice parameter is approximately 4.35 Å, in good agreement with the value calculated from the Rietveld refinement (4.352 Å). The high-angle annular dark-field (HAADF) STEM image combined with the corresponding EDS elemental maps (Fig. 2(g)) further illustrates a homogeneous distribution of constituent elements, and no evidence of phase segregation regions is detected, indicating excellent compositional uniformity of the solid solution. The five transition metal elements (Ti, V, Nb, Ta, and Mo) exhibit equiatomic ratios and are uniformly distributed at the nanoscale. Only a trace amount of Al, approximately 0.01 at%, was detected within the lattice. For comparison, the nominal Al content in the initial batching composition corresponds to approximately 0.18 at%, suggesting that the solid solubility of Al in the high-entropy carbide lattice is thermodynamically feasible but limited [30]. Additionally, as illustrated in Figs. 2(d)–2(f), a small amorphous Al_2O_3 region is also observed and embedded within the crystalline matrix. The high-resolution TEM (HRTEM) image clearly reveals a sharp boundary between the ordered lattice and the amorphous domain, indicating local oxidation of Al inside the grain during sintering. Notably, neither partially oxidized Al nor any enrichment of Al-bearing compounds is observed along the grain boundaries, which is inconsistent with the typical features of liquid-phase sintering.

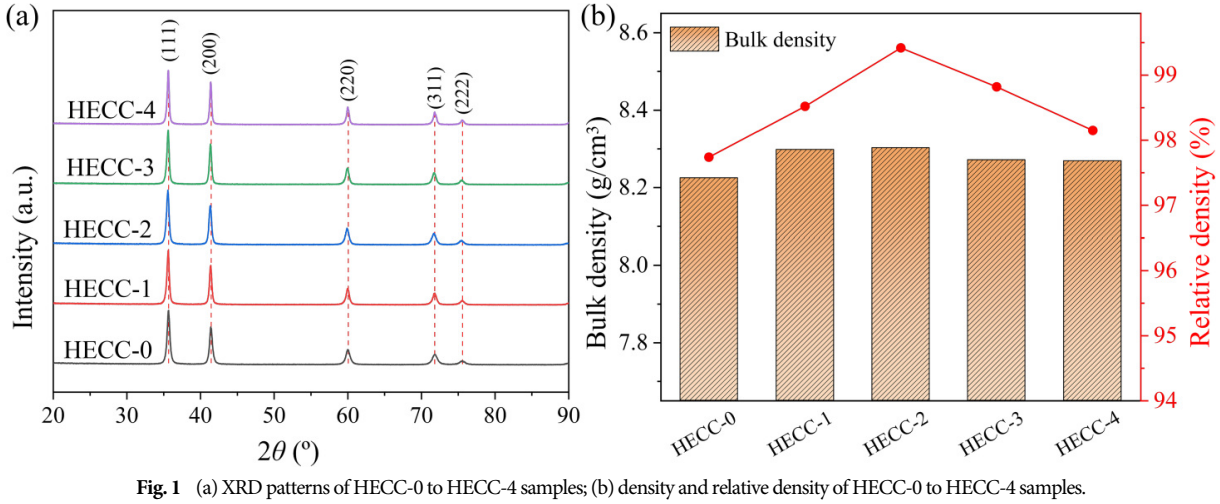

Fig. 1 (a) XRD patterns of HECC-0 to HECC-4 samples; (b) density and relative density of HECC-0 to HECC-4 samples.

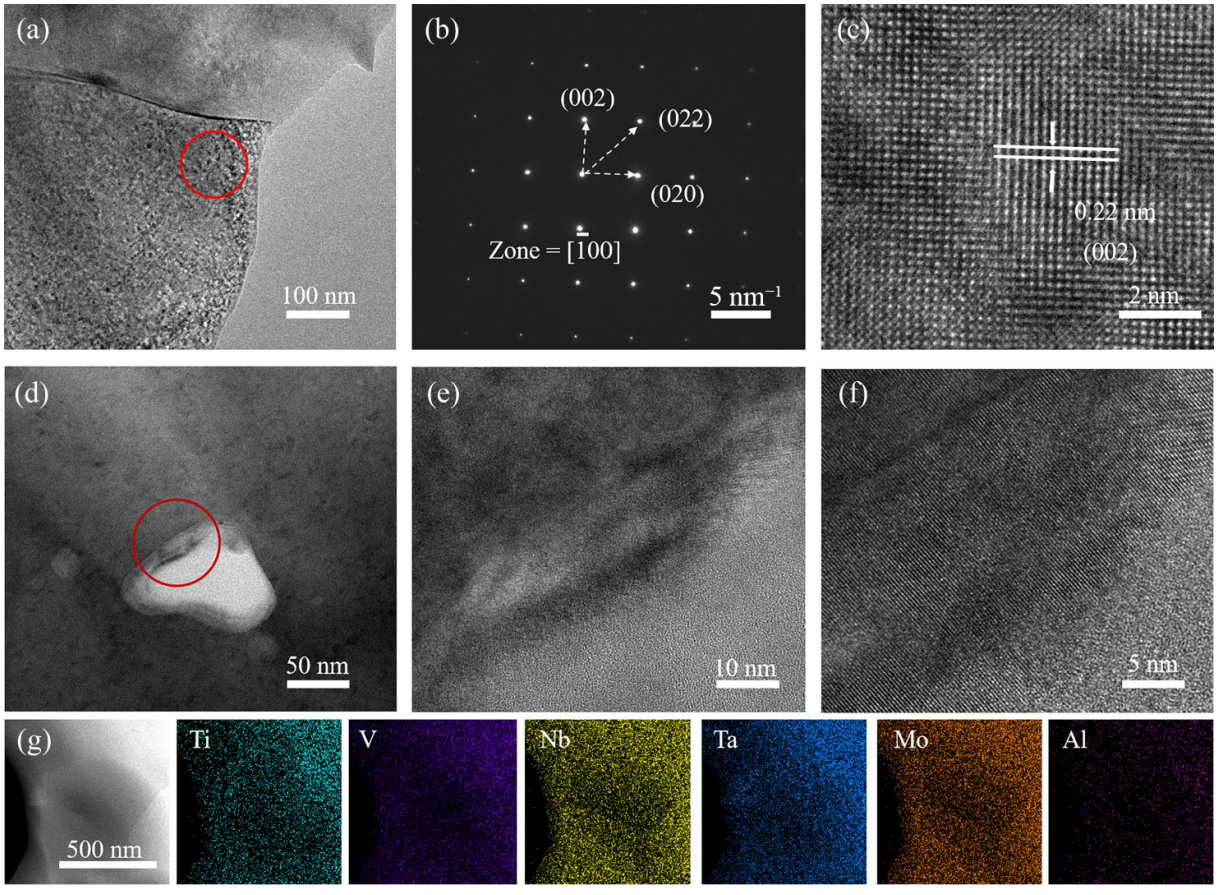

Fig. 2 TEM characterization of the HECC-1 sample: (a) bright-field TEM image; (b) selected area electron diffraction pattern; (c) high-resolution TEM image; (d–f) bright-field and high-resolution TEM images of amorphous Al_2O_3 area; (g) STEM image and corresponding EDS elemental mapping of Ti, V, Nb, Ta, Mo, and Al.

The chemical states and bonding configurations of the constituent elements in HECC-1 were further examined by XPS. The XPS survey spectrum confirms the presence of Ti, V, Nb, Ta, Mo, Al, and C. The high-resolution spectra of the C 1s, Ti 2p, V 2p, Nb 3d, Ta 4f, and Mo 3d regions with their corresponding fitted components are shown in Fig. 3. While trace Al peaks were observed, the spectra were dominated by noise, making it impossible to extract meaningful chemical information. The C 1s spectrum, as shown in Fig. 3(a), exhibits a dominant peak at ~282.03 eV corresponding to C–TM (TM = Ti, V, Nb, Ta, Mo) covalent bonds and a weak shoulder at ~284.80 eV assigned to C–C bonds, indicating only a small fraction of amorphous carbon. In the Ti 2p region, two main peaks at ~454.31 eV (Ti $2p_{3/2}$) and ~462.93 eV (Ti $2p_{1/2}$) are assigned to Ti–C bonds, and another pair of peaks located at ~459.71 and ~466.33 eV corresponds to Ti–O bonds, indicating the presence of a thin oxidized layer on the surface. The V 2p spectrum consists of two spin-orbit doublets corresponding to V–C and V–O bonds. The peaks at ~512.45 eV (V $2p_{3/2}$) and ~520.02 eV (V $2p_{1/2}$) are assigned to V–C bonding, whereas another pair at ~514.35 and ~523.07 eV is attributed to V–O species, indicating that vanadium exists in both carbide and oxide states due to slight surface oxidation. The Nb 3d and Ta 4f spectra are dominated by M–C bonds at ~202.87/205.62 and ~22.43/24.35 eV, respectively, each showing a weak high-energy shoulder indicative of trace oxidation. The Mo 3d spectrum exhibits two main peaks at ~227.67 and ~230.94 eV, assigned to Mo–C, along with a pair of low-energy peaks (~225.63/229.55 eV) corresponding to metallic Mo^0 or carbon-deficient MoC_x. Overall, the XPS results confirm that Ti, V, Nb, Ta, and Mo primarily exist in carbide states with only minor surface oxidation. The pronounced Ti–O and V–O features together with the weak Mo–metallic signal indicate slight surface oxidation and carbon nonstoichiometry, originating from the design of the starting materials and contributing to the formation of localized hybrid covalent–metallic bonding states.

3.2 Microstructures of (TiVNbTaMo)C_x

The lattice parameters of HECC-1 to HECC-4 were determined by Rietveld refinement to be 4.352, 4.364, 4.359, and 4.350 Å, as shown in Fig. S3 in the ESM. The lattice parameter of HECC-0 was reported to be 4.355 Å [31]. Based on these values, the theoretical densities were calculated and compared with the experimental bulk densities measured by the Archimedes method (Fig. 1(b)). The relative densities of HECC 0–4 range from 97.7% to 99.4%, exhibiting a volcano-type dependence on Ti_3AlC_2 content that first increases and then decreases, reaching a maximum at HECC-2.

SEM micrographs of the high-entropy carbide ceramics (HECC 1–4) and the corresponding energy-dispersive spectroscopy (EDS) elemental mappings are presented in Fig. S4 in the ESM. EDS elemental maps reveal that Ti, V, Nb, Ta, Mo, and Al are predominantly uniformly distributed within the matrix of all HECC0–4 samples. The dark regions appearing on the surface are consistent with the slight aggregation tendency of Ti, which might be caused by the formation of Ti oxides. Despite the relative densities being slightly below 100%, the polished surfaces appear pore-free, indicating dense structures. A gradual homogenization of the transition metal elements (Ti, V, Nb, Ta, and Mo) and carbon distribution is observed with the increasing addition of Ti_3AlC_2. In contrast, Al shows a tendency toward segregation due

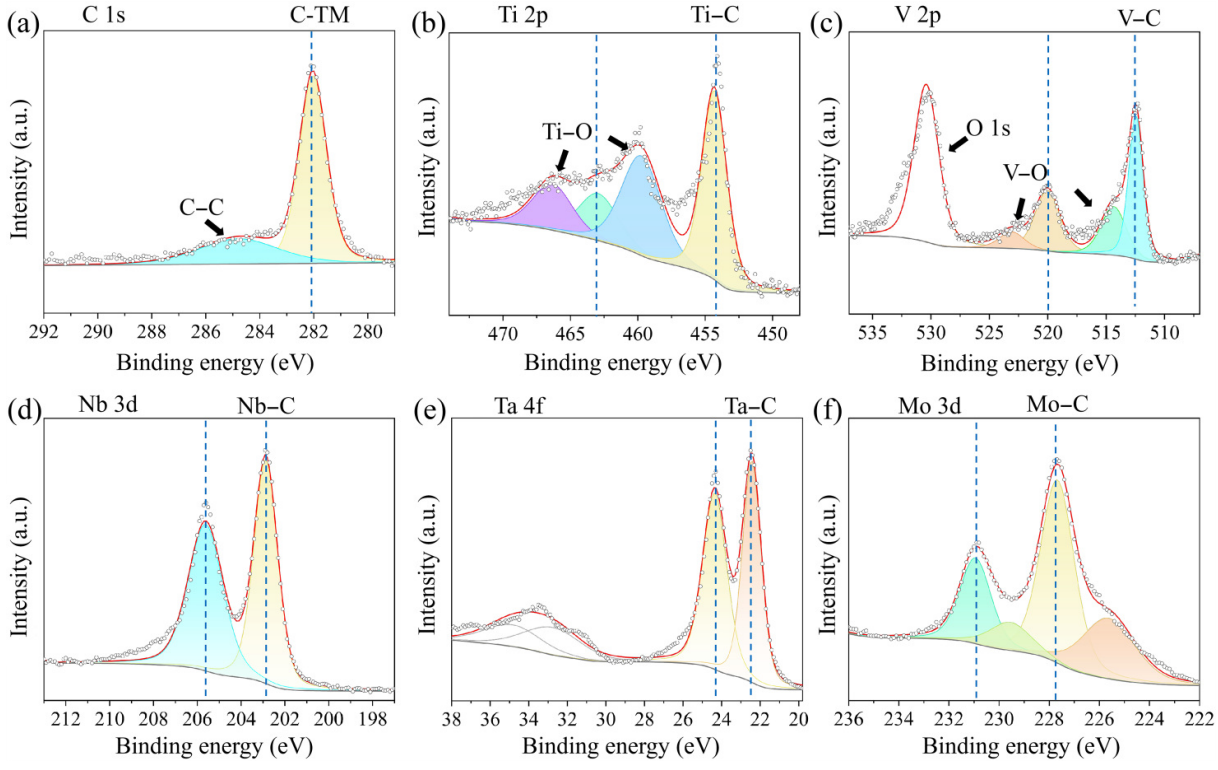

Fig. 3 XPS spectra of (a) C 1s, (b) Ti 2p, (c) V 2p, (d) Nb 3d, (e) Ta 4f, and (f) Mo 3d for HECC-1.

to its limited solubility in the carbide lattice, as discussed in Section 3.1. The excess Al locally accumulates, and its distribution coincides with oxygen enrichment, indicating that surface Al is prone to oxidation. These Al–O regions are discontinuous and aggregated rather than forming a compact layer. The surface Al concentrations measured by EDS were 0.06, 0.19, 0.35, and 0.65 at% for HECC-1–4, respectively, which follow the same increasing trend as the nominal Al contents introduced by Ti_3AlC_2 addition (0.18, 0.35, 0.53, and 0.71 at%), suggesting partial Al loss or segregation during sintering [32].

The fracture surface morphologies of the HECC 0–4 samples are illustrated in Fig. 4. The fracture surfaces exhibit typical brittle fracture characteristics, without any ductile dimples or signs of plastic deformation. They display a mixed intergranular–transgranular fracture mode, characterized by distinct grain boundaries and step-like facets. The grain sizes of the HECC-0–4 samples were statistically evaluated from cross-sectional SEM images, yielding average values of 0.71, 0.68, 0.69, 0.80, and 1.03 μm, respectively. HECC-1 exhibits a smaller average grain size and a more uniform size distribution than the other samples. The limited liquid phase formed at this stage can effectively wet grain boundaries and pin grain growth, resulting in a finer and more uniform microstructure [33–35]. With increasing Ti_3AlC_2 content, excessive formation of transient liquid or secondary phases accelerates diffusion and coalescence of grains, weakening the pinning effect and leading to rapid grain coarsening [36]. Consequently, moderate Ti_3AlC_2 addition (HECC-1) optimizes the balance between densification and grain growth, while higher additions promote excessive grain coarsening.

Additionally, all samples exhibit relatively dense microstructures without visible large pores or delamination, confirming effective densification during reactive sintering. Several isolated micropores are still observed, which are likely residual voids generated during phase evolution and solid-state diffusion. The variation in macrovoids with increasing Ti_3AlC_2 content exhibits a nonmonotonic trend, which decreases initially (HECC-1 and HECC-2) due to enhanced sintering activity but increases again at higher Ti_3AlC_2 contents. The HECC-1 and HECC-2 specimens exhibit smooth and compact fracture surfaces with well-bonded grains and clearly defined boundaries. In contrast, the HECC-3 and HECC-4 samples show rougher surfaces with blurred grain boundaries and scattered particle-like agglomerates. The coexistence of these unstable regions and residual pores can be explained by the decomposition of Ti_3AlC_2 and the high mobility of Al during sintering, which tends to induce local structural fluctuations [28].

3.3 Mechanical properties of (TiVNbTaMo)C_x

The flexural strength, fracture toughness, and Vickers hardness of the HECC 0–4 samples are summarized in Fig. 5(a). The flexural strength exhibits a clear compositional dependence. HECC-1 shows the highest flexural strength (~1018 MPa), while the relatively short error bars suggest good structural uniformity and consistent mechanical behavior. With a further increase in the Ti_3AlC_2 content, the flexural strength gradually decreases, and the error bars become noticeably larger. This tendency agrees well with the microstructural features shown in Fig. 4 and discussed in Section 3.2. The Vickers hardness under a load of 9.8 N increases with the addition of Ti_3AlC_2 up to a certain point, reaching its maximum in the HECC-2 sample, and then remains constant. In contrast, the Vickers hardness under a load of 0.49 N (Fig. S6 in the ESM) and the fracture toughness follow a trend similar to that of flexural strength, reaching their respective maxima of 41.40 GPa and 5.67 MPa·$m^{1/2}$ in the HECC-1 sample. Although monolithic ceramics often exhibit a trade-off between strength and fracture toughness, the simultaneous enhancement observed in HECC-1 compared with HECC-0 can be attributed to subtle but effective microstructural refinements. Specifically, HECC-1 exhibits a higher degree of densification with reduced residual porosity, which lowers stress concentration and crack-initiation sites, thereby benefiting both flexural strength and fracture toughness. In addition, the aluminum generated from the

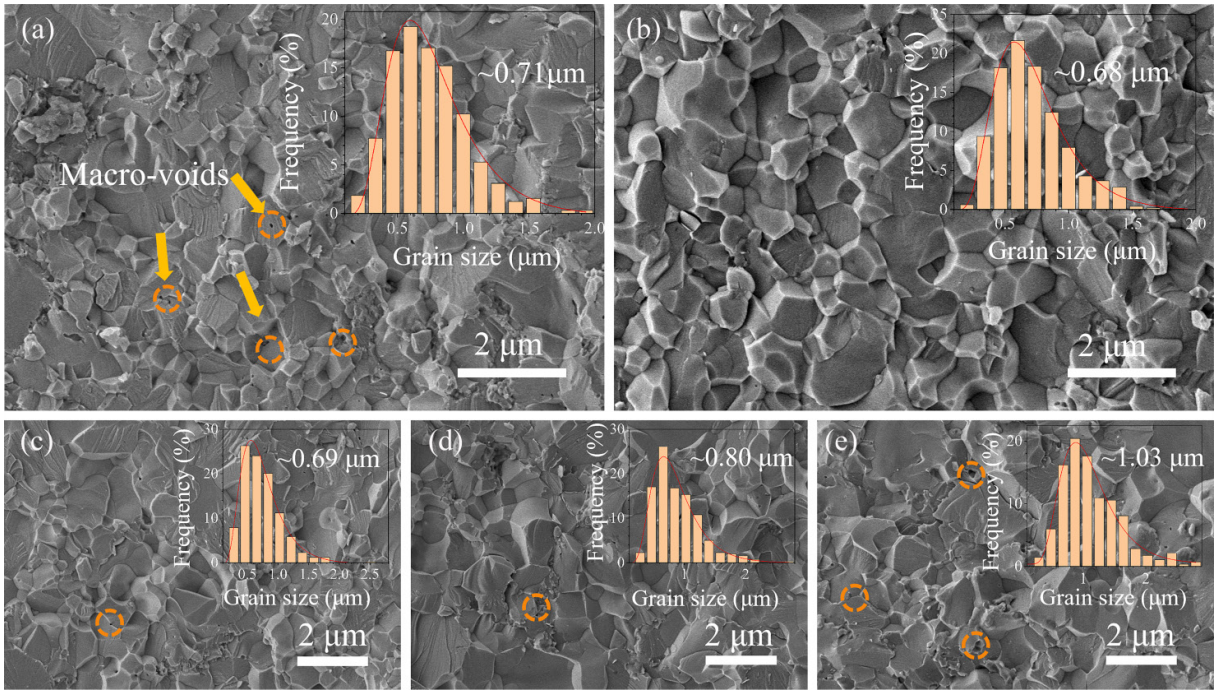

Fig. 4 Morphology of the fracture surface and corresponding grain size distribution: (a) HECC-0; (b) HECC-1; (c) HECC-2; (d) HECC-3 and (e) HECC-4.

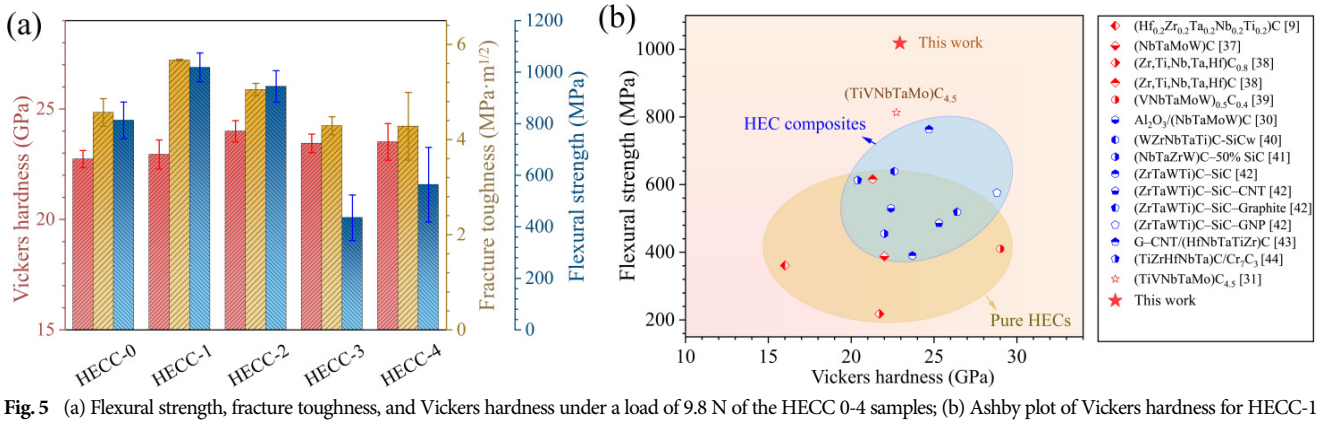

Fig. 5 (a) Flexural strength, fracture toughness, and Vickers hardness under a load of 9.8 N of the HECC 0-4 samples; (b) Ashby plot of Vickers hardness for HECC-1 compared with previously reported high-entropy ceramics [9,30,31,37–44].

decomposition of Ti_3AlC_2 plays a dual role. It reduces the surface oxide layers on the ceramic particles, promoting mass transport during sintering and facilitating densification. Moreover, a small amount of Al or its oxide, distributed along the grain boundaries, provides a pinning effect during grain growth, leading to grain refinement. According to the Hall–Petch relationship (Eq. (1)), the hardness increases with decreasing average grain size. Therefore, a smaller grain size is beneficial for improving the hardness. In addition to the intrinsic solid-solution strengthening, the improved compactness and structural integrity in the HECC sample may further contribute to the overall strengthening of the mechanical properties. Interestingly, a trade-off between grain size and densification is observed, with finer grains contributing more significantly to the enhancement of mechanical properties than further densification. Therefore, the relatively dense and fine-grained HECC-1 exhibits excellent mechanical properties, with the Vickers hardness and flexural strength surpassing those of many previously reported high-entropy carbides and related composites, as shown in the Ashby-type plot in Fig. 5(b).

Vickers indentation tests were conducted under a load of 9.8 N to investigate the crack propagation behavior and fracture characteristics of the obtained samples. Well-defined impressions with sharp edges and radial cracks can be clearly observed, as shown in Fig. 6. The crack propagation patterns around the indents were examined to elucidate the corresponding toughening mechanisms. In HECC-1 and HECC-2, several fine zig-zag cracks were observed, accompanied by multiple crack interaction modes, including blunting, deflection, and bridging, indicating effective crack-tip shielding and improved fracture resistance [45]. In HECC-3 and HECC-4, the zig-zag cracks become wider and fewer in comparison. Although the dense microstructure induces limited crack deflection and energy dissipation during crack propagation, no distinct toughening mechanisms, such as particle pull-out, were observed. This indicates that the apparent toughness improvement mainly arises from the densified and uniform microstructure rather than intrinsic toughening effects, suggesting that the intrinsic fracture resistance still offers considerable room for further optimization [45–47].

3.4 Tribological properties of high-entropy (TiVNbTaMo)C_x

High-temperature friction and wear behavior is a critical factor governing the reliability and durability of structural ceramics

operating under extreme environments [48]. Elevated temperatures often induce oxidation, interfacial reactions, and microstructural evolution, which can significantly modify the surface frictional response [49,50]. Therefore, examining tribological behavior at high temperatures is essential for understanding the surface stability of materials. In this part, the tribological properties of HECC-0 and HECC-1 were systematically evaluated to elucidate how the Ti_3AlC_2 activator affects their high-temperature frictional response and wear mechanisms.

The coefficient of friction (COF) curves, along with the average COF values and wear rates of the HECC-0 and HECC-1 samples at various temperatures (RT–900 °C), are presented in Fig. 7. As shown in Fig. 7(a), the COF of HECC-0 changes markedly with temperature, decreasing from 0.53 at room temperature to 0.39 at 600 °C and rising again at 900 °C. In contrast, the HECC-1 (Fig. 7(c)) sample shows a nearly constant COF (0.55–0.63) over the whole temperature range. The wear rates of the (TiVNbTaMo)C_x high-entropy carbide ceramics are summarized in Figs. 7(b) and 7(d). For HECC-0, the wear rates were $(1.53\pm0.79)\times10^{-6}$ mm³/(N·m) at room temperature and $(1.70–3.30)\times10^{-5}$ mm³/(N·m) from 300 to 900 °C, showing a

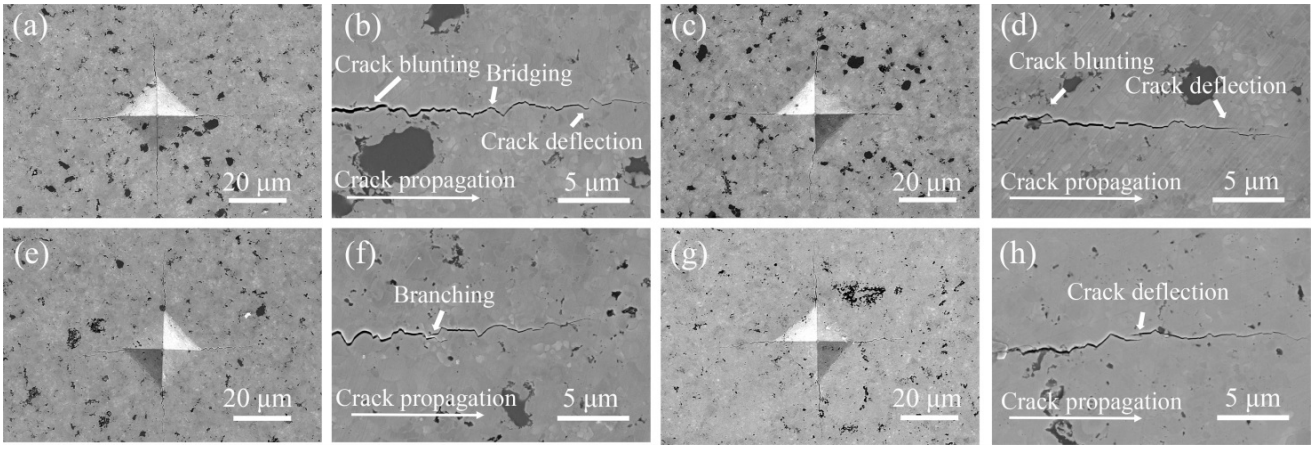

Fig. 6 SEM images of the Vickers indentation morphology under a load of 9.8 N: (a, b) HECC-1; (c, d) HECC-2; (e, f) HECC-3; and (g, h) HECC-4.

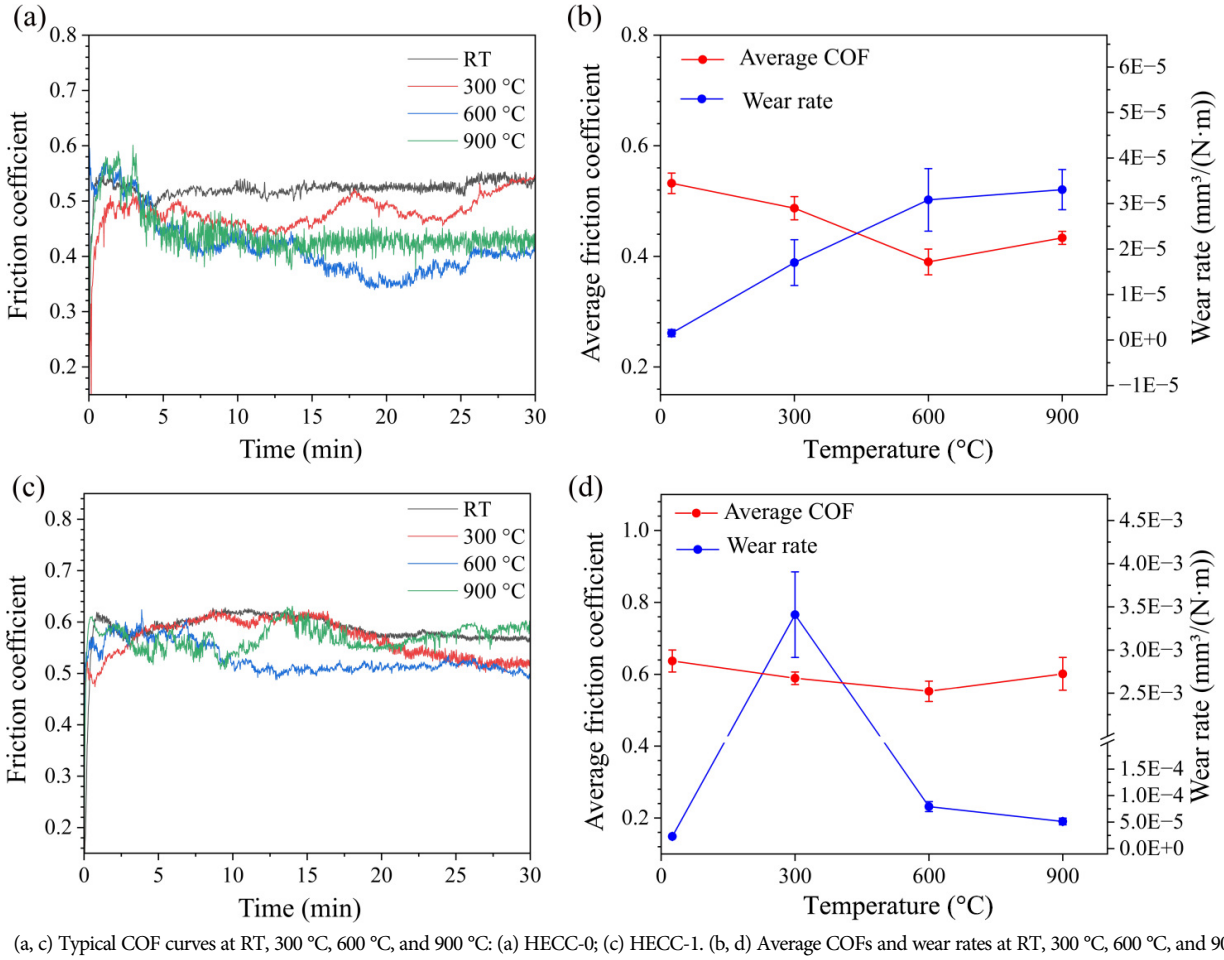

Fig. 7 (a, c) Typical COF curves at RT, 300 °C, 600 °C, and 900 °C: (a) HECC-0; (c) HECC-1. (b, d) Average COFs and wear rates at RT, 300 °C, 600 °C, and 900 °C: (b) HECC-0; (d) HECC-1.

generally stable trend with only a slight increase at elevated temperatures. For HECC-1, the wear rates were $(2.31\pm0.22)\times10^{-5}$, $(3.41\pm0.50)\times10^{-3}$, $(7.92\pm0.94)\times10^{-5}$, and $(5.12\pm0.63)\times10^{-5}$ $mm^3/(N\cdot m)$ at RT, 300 °C, 600 °C, and 900 °C, respectively. The wear rates were generally stable at different temperatures, except for a distinct increase observed at 300 °C. The wear scars on the counterpart balls were examined by SEM, and the corresponding diameters are summarized in Table 2. HECC-1 produced a larger wear mark than HECC-0, accompanied by distinct abrasive features.

The worn-surface morphologies and elemental distributions were analyzed by SEM and EDS, respectively, and the 3D surface topographies further revealed the wear-track profiles of HECC-0 and HECC-1, as illustrated in Fig. 8 and Fig. S5 in the ESM, respectively. Under vacuum conditions, all samples exhibit certain common tribological features, including limited oxygen participation, partial material transfer from the Si_3N_4 counterpart, and the gradual formation of Si–O–M (M = Ti, Nb, Mo, and Ta) mixed species within the wear tracks [51]. However, the dominant wear mechanism evolves markedly with temperature.

Table 2 Wear scar diameters of HECC-0 and HECC-1 samples at different temperatures (Unit: μm)

Sample	Temperature			
	RT	300 °C	600 °C	900 °C
HECC-0	761	578	671	778
HECC-1	1013	2027	967	753

At room temperature, HECC-0 undergoes mechanical abrasion accompanied by third-body transfer. Nb and Mo are locally enriched beneath the unworn regions with only trace oxygen, whereas Si and O are concentrated on the worn track due to transfer or oxidation of the Si_3N_4 counterpart. Such direct asperity contact results in a high and strongly fluctuating friction coefficient. At 300–600 °C, the friction coefficient shows pronounced oscillations, which can be attributed to the formation and repeated rupture of a thin, discontinuous oxide film. This transient layer provides intermittent protection but lacks sufficient adhesion and mechanical integrity. Continuous oxidation and debris transfer promote cyclic regeneration of the film, leading to a dynamically unstable yet gradually improving surface condition. When the testing temperature is raised to 900 °C, the surface is covered by a compact and adherent composite film with Nb-/Ta-

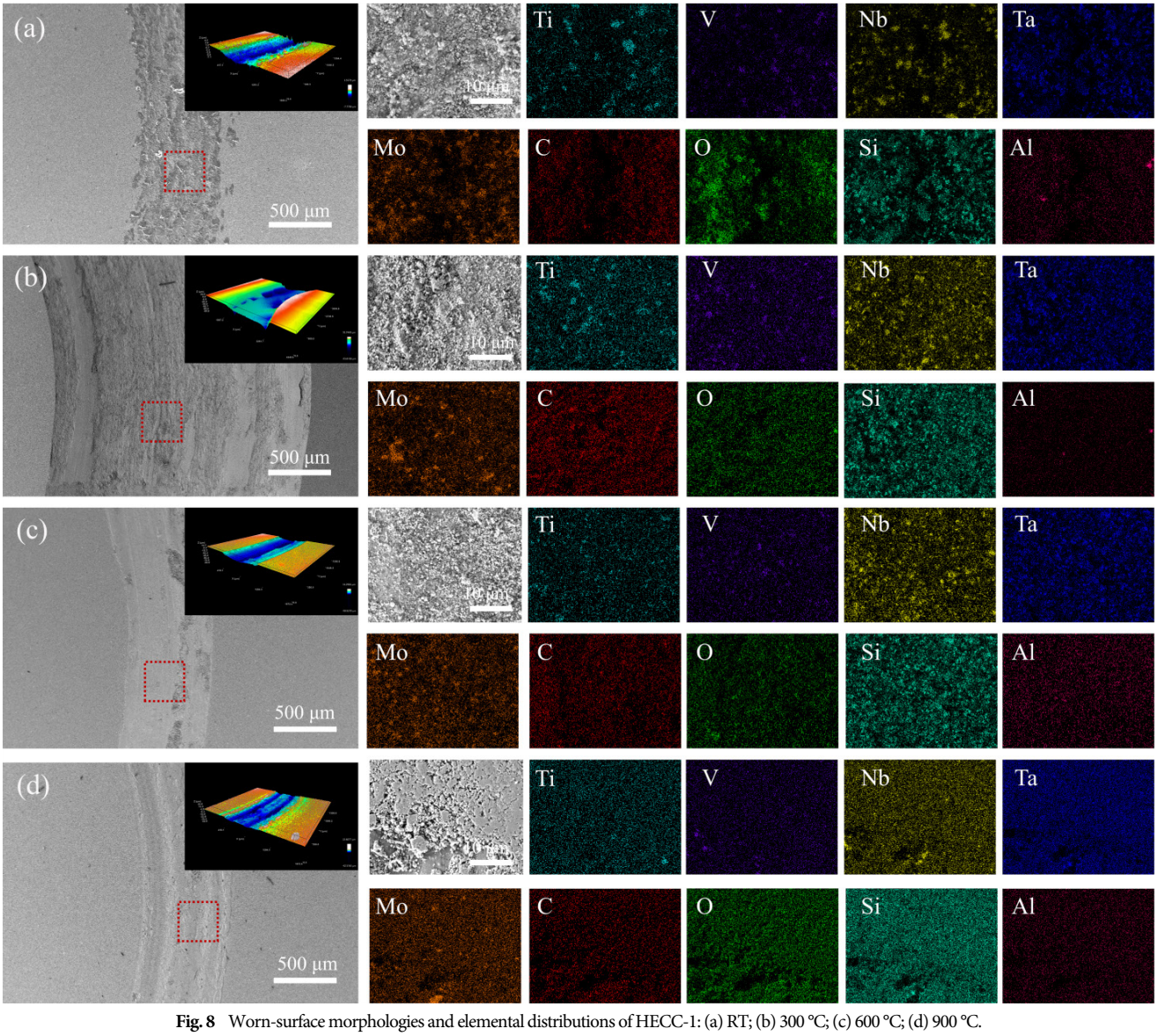

Fig. 8 Worn-surface morphologies and elemental distributions of HECC-1: (a) RT; (b) 300 °C; (c) 600 °C; (d) 900 °C.

rich regions and Mo- and V-containing species. The Nb- and Ta-rich oxides provide strong adhesion and structural stability, whereas the Mo- and V-oxides possess intrinsic layered or low-shear characteristics, contributing to the lubricious nature of the film, as reported in previous studies [52–54]. This continuous oxide layer effectively separates the contact surfaces, resulting in a pronounced reduction and long-term stabilization of the friction coefficient, accompanied by a low wear rate, as illustrated in Fig. 9(d).

Compared with HECC-0, HECC-1 exhibits a rougher worn surface at room temperature, characterized by pronounced delamination and debris accumulation, indicative of severe abrasive–adhesive wear. Elemental mapping shows that Si and the transition metal elements (Ti, V, Nb, Ta, and Mo) exhibit nearly identical spatial distributions across the worn surface, suggesting a uniform removal of the surface layer rather than localized segregation. At 300 °C, the wear track becomes noticeably wider and deeper, indicating a temporary deterioration in wear resistance before the formation of a stable protective film. The oxygen-deficient vacuum environment suppresses oxidation, hindering the formation of a continuous tribo-oxide film. The combination of strong mechanical contact and enhanced atomic-scale adhesion under vacuum promotes repeated adhesion–spallation cycles. At elevated temperatures, the HECC-1 sample exhibits an effective reduction in interfacial shear and stabilization of the friction behavior. Furthermore, the Si_3N_4 counterpart shows a smooth surface without adherent deposits, indicating that the tribolayer is mainly retained on the ceramic surface rather than transferred across the friction pair, as presented in Fig. 9(h).

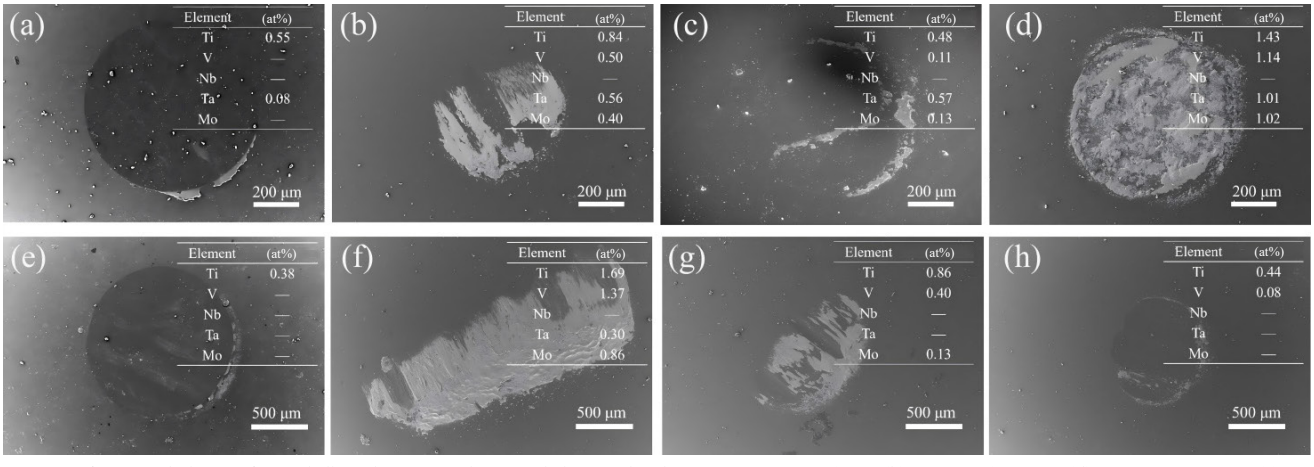

Fig. 9 Surface morphologies of Si_3N_4 balls and corresponding metal element distribution. HECC-0 at (a) RT; (b) 300 °C; (c) 600 °C; (d) 900 °C. HECC-1 at (e) RT; (f) 300 °C; (g) 600 °C; (h) 900 °C.

The minor amount of Al introduced by Ti_3AlC_2 modification exerts a significant influence on the high-temperature tribological behavior. During sliding, Al facilitates the formation of a discontinuous and easily spallable oxide film. The repeated formation and detachment of this film continuously renews the contact surface, suppressing the accumulation of wear debris and maintaining a steady friction coefficient over a wide temperature range. Meanwhile, the inherently high strength and hardness of the ceramic matrix effectively limit the overall wear loss, preventing severe surface damage. Therefore, the addition of Ti_3AlC_2 modifies the surface condition and enhances adhesive wear, leading to an increase in the wear volume of the sample. Despite the increased wear volume, HECC-1 maintains stable and smooth frictional behavior at elevated temperatures, demonstrating potential for use in high-temperature wear-resistant components where a balance of wear resistance and friction stability is crucial [55–57].

4 Conclusions

This work introduces a Ti_3AlC_2-assisted reaction sintering strategy that enables efficient low-temperature densification of high-entropy carbide ceramics. The reactive decomposition of Ti_3AlC_2 simultaneously accelerates interdiffusion via in situ-formed TiC_x and activates particle interfaces through Al release, resulting in rapid densification and microstructural refinement. A nearly fully dense high entropy sample was achieved in the sample with 0.6 wt% Ti_3AlC_2 addition due to the strong sintering-promoting effect of Ti_3AlC_2 during reactive in situ consolidation. The resulting sample exhibits a Vickers hardness of 22.94 GPa and a flexural strength of 1018 MPa, both comparable to those of state-of-the-art high-entropy carbides, together with moderate toughness. Additionally, interfacial modification during sintering promotes stable friction and nonadhesive wear behavior under elevated temperatures, indicating its potential application in high-temperature wear-resistant components. In summary, the reactive in situ sintering approach provides a general and energy-efficient route for fabricating dense and strong high-entropy carbides.

Acknowledgements

This work was supported by the National Natural Science Foundation of China (Nos. U23A20562, 52172075, and 52402079); the Henan Province University Science and Technology Innovation Team Support Program (No. 23IRTSTHN001); Henan Province Major Basic Research Program (No. 252310420100); Henan Provincial Science and Technology Research Project (No. 252102231065).

Author contributions

Jingwen Song: Writing – original draft, visualization, validation, software, methodology, formal analysis. Mingliang Li: Writing – review & editing, methodology. Hailong Wang: Writing – review & editing, supervision, resources, methodology, funding acquisition, conceptualization. Pengbo Zhao: Writing –review & editing, funding acquisition. Ziqi Zhao: Writing –review & editing. Wei Li: Writing – review & editing, visualization, investigation, funding acquisition, data curation. Kehao Zhang:

Writing –review & editing. Kai Zhang: Writing –review & editing. Rui Zhang: Writing – review & editing, supervision. All the authors have approved the final manuscript.

Availability of data and materials

The data that support the findings of this study are available from the corresponding author upon reasonable request.

Competing interests

The authors have no competing interests to declare that are relevant to the content of this article.

Electronic Supplementary Material

Supplementary material is available in the online version of this article at https://doi.org/10.26599/JAC.2026.9221242.

References

[1] Xiang HM, Xing Y, Dai FZ, *et al.* High-entropy ceramics: Present status, challenges, and a look forward. *J Adv Ceram* 2021, **10**: 385–441.

[2] Feng L, Fahrenholtz WG, Brenner DW. High-entropy ultra-high-temperature borides and carbides: A new class of materials for extreme environments. *Annu Rev Mater Res* 2021, **51**: 165–185.

[3] Wyatt BC, Nemani SK, Hilmas GE, *et al.* Ultra-high temperature ceramics for extreme environments. *Nat Rev Mater* 2024, **9**: 773–789.

[4] Smith SM II, Fahrenholtz WG, Hilmas GE, *et al.* Intermediate stage densification kinetics of high-entropy ceramics during spark plasma sintering. *J Eur Ceram Soc* 2025, **45**: 117136.

[5] Cao ZN, Sun JL, Meng LT, *et al.* Progress in densification and toughening of high entropy carbide ceramics. *J Mater Sci Technol* 2023, **161**: 10–43.

[6] Sarker P, Harrington T, Toher C, *et al.* High-entropy high-hardness metal carbides discovered by entropy descriptors. *Nat Commun* 2018, **9**: 4980.

[7] Castle E, Csanádi T, Grasso S, *et al.* Processing and properties of high-entropy ultra-high temperature carbides. *Sci Rep* 2018, **8**: 8609.

[8] Csanádi T, Castle E, Reece MJ, *et al.* Strength enhancement and slip behaviour of high-entropy carbide grains during micro-compression. *Sci Rep* 2019, **9**: 10200.

[9] Yu D, Zhang BH, Yin J, *et al.* Densifying $(Hf_{0.2}Zr_{0.2}Ta_{0.2}Nb_{0.2}Ti_{0.2})C$ high-entropy ceramics by two-step pressureless sintering. *J Am Ceram Soc* 2022, **105**: 76–81.

[10] Zhang W, Chen L, Xu CG, *et al.* Grain growth kinetics and densification mechanism of (TiZrHfVNbTa)C high-entropy ceramic under pressureless sintering. *J Mater Sci Technol* 2022, **110**: 57–64.

[11] Bai XY, Sun Y, Cheng ZY, *et al.* Ultrafast pressure sintering: A one-step route to dense high-entropy carbide from precursors. *J Eur Ceram Soc* 2025, **45**: 117095.

[12] An HB, Chen RY, Li SS, *et al.* Influence of (TaNbTiV)C powders synthesized by molten salt at low temperature on densification and properties of high entropy carbide ceramics. *J Am Ceram Soc* 2024, **107**: 4679–4688.

[13] Chen L, Zhang W, Lu WY, *et al.* Low thermal conductivity of dense $(TiZrHfVNbTa)C_x$ high-entropy carbides by tailoring carbon stoichiometry. *J Adv Ceram* 2023, **12**: 49–58.

[14] Zhang W, Chen L, Lu WY, *et al.* Non-stoichiometry of (TiZrHfVNbTa)C and its significance to the microstructure and mechanical properties. *J Eur Ceram Soc* 2022, **42**: 6347–6355.

[15] Hu JJ, Zhang Y, Yan DS, *et al.* Unveiling the role of carbon vacancies in microstructure evolution and mechanical properties of high-entropy carbides. *J Eur Ceram Soc* 2025, **45**: 117080.

[16] Wang F, Zhang X, Yan XL, *et al.* The effect of submicron grain size on thermal stability and mechanical properties of high-entropy carbide ceramics. *J Am Ceram Soc* 2020, **103**: 4463–4472.

[17] Feng L, Fahrenholtz WG, Hilmas GE. Low-temperature sintering of single-phase, high-entropy carbide ceramics. *J Am Ceram Soc* 2019, **102**: 7217–7224.

[18] Liu Y, Liang JJ, Guo WM, *et al.* Cr-assisted low-temperature densification of (Ti,Zr,Nb,Ta,Mo)C high-entropy carbides with ultrafine grain and enhanced hardness. *J Adv Ceram* 2024, **13**: 780–788.

[19] He YQ, Liu ZH, Zhang BH, *et al.* Dual sinter-aids to fabricate high-entropy transition metal carbide ceramic and their properties. *Ceram Int* 2024, **50**: 28899–28906.

[20] Wang YC, Cheng ZL, Girman V, *et al.* High-temperature compressive behaviour and failure mechanism of high entropy carbides modified by Cr addition. *Mater Sci Eng A* 2025, **920**: 147532.

[21] Su WT, Chen L, Zhang W, *et al.* Insights into grain boundary segregation and solubility limit of Cr in (TiZrNbTaCr)C. *J Mater Sci Technol* 2023, **139**: 1–9.

[22] Anwer Z, Huang SG, Vleugels J. Liquid phase assisted synthesis of (Ti,V,Nb,Ta,W)C–Ni high entropy carbide cermets by conventional pressureless sintering. *Int J Refract Met Hard Mater* 2022, **107**: 105914.

[23] Deng XC, Zhang GH. Preparation of high-performance (ZrHfTaNbTiMo)C–10Co ceramic by SPS using self-synthesized fine high-entropy carbide powders. *Ceram Int* 2024, **50**: 21050–21058.

[24] Wang XC, Saunders TG, Sedlák R, *et al.* Synthesis and densification of (Zr–Hf–Nb–Ta)C–Co high entropy cermet prepared by pressureless melt infiltration using spark plasma sintering. *J Alloys Compd* 2022, **900**: 163412.

[25] Zheng LY, Li FZ, Zhou YC. Preparation, microstructure, and mechanical properties of TiB_2 using Ti_3AlC_2 as a sintering aid. *J Am Ceram Soc* 2012, **95**: 2028–2034.

[26] Lu XP, Zhou YC. Pressureless sintering and properties of Ti_3AlC_2. *Int J Appl Ceram Technol* 2010, **7**: 744–751.

[27] Ji CC, Wang HL, Li ML, *et al.* Microstructure and mechanical properties of high-entropy diboride-based ceramic assisted by Ti_3AlC_2 additive. *Ceram Int* 2024, **50**: 30810–30820.

[28] Pietzka MA, Schuster JC. Summary of constitutional data on the aluminum–carbon–titanium system. *J Phase Equilib* 1994, **15**: 392–400.

[29] Epifano E, Monceau D. Ellingham diagram: A new look at an old tool. *Corros Sci* 2023, **217**: 111113.

[30] Liu DQ, Zhang AJ, Jia JG, *et al.* A novel *in-situ* exothermic assisted sintering high entropy Al_2O_3/(NbTaMoW)C composites: Microstructure and mechanical properties. *Compos Part B Eng* 2021, **212**: 108681.

[31] Song JW, Wang HL, Li W, *et al.* Low-temperature consolidation of high-entropy $(TiVNbTaMo)C_{4.5}$ ceramics with exceptional strength and hardness. *Nano Res* 2025, **18**: 94908008.

[32] Chen G, Cao P, He YH, *et al.* Effect of aluminium evaporation loss on pore characteristics of porous FeAl alloys produced by vacuum sintering. *J Mater Sci* 2012, **47**: 1244–1250.

[33] Yoon BK, Choi SY, Yamamoto T, *et al.* Grain boundary mobility and grain growth behavior in polycrystals with faceted wet and dry boundaries. *Acta Mater* 2009, **57**: 2128–2135.

[34] Song K, Aindow M. Grain growth and particle pinning in a model Ni-based superalloy. *Mater Sci Eng A* 2008, **479**: 365–372.

[35] Cheng YY, Zhou L, Liu JX, *et al.* Grain growth inhibition by sluggish diffusion and Zener pinning in high-entropy diboride ceramics. *J Am Ceram Soc* 2023, **106**: 4997–5004.

[36] Xie H, Qin MD, Hong M, *et al.* Rapid liquid phase-assisted ultrahigh-temperature sintering of high-entropy ceramic composites. *Sci Adv* 2022, **8**: eabn8241.

[37] Liu DQ, Zhang AJ, Jia JG, *et al.* Reaction synthesis and characterization of a new class high entropy carbide (NbTaMoW)C. *Mater Sci Eng A* 2021, **804**: 140520.

[38] Tan YQ, Liao W, Teng Z, *et al.* Synthesis, mechanical, and thermophysical properties of high-entropy $(Zr,Ti,Nb,Ta,Hf)C_{0.8}$ ceramic. *J Am Ceram Soc* 2023, **106**: 4382–4389.

[39] Liu DQ, Hou YQ, Meng JH, *et al.* The significant influence of carbon

content on mechanical and thermal properties of $(VNbTaMoW)_{0.5}C_x$ high entropy carbides. *J Eur Ceram Soc* 2022, **42**: 5262–5272.
[40] Zhang JT, Wang WL, Zhang ZX, *et al.* Synthesis, microstructure, mechanical and tribological properties of high-entropy carbides (WZrNbTaTi)C–SiC_w. *Ceram Int* 2024, **50**: 50780–50792.
[41] Peng F, Wei Z, Song QQ, *et al.* Simultaneous hardening and toughening of a high-entropy (NbTaZrW)C ceramic carbide using SiC particle. *J Am Ceram Soc* 2023, **106**: 4443–4454.
[42] Rana D, Balani K. Isolating strengthening contributions in multiphase high entropy (Zr–Ta–W–Ti)C–SiC based carbide ceramics. *Int J Refract Met Hard Mater* 2023, **110**: 106024.
[43] Sun JL, Zhao J, Zhou YH, *et al.* High-performance multifunctional $(Hf_{0.2}Nb_{0.2}Ta_{0.2}Ti_{0.2}Zr_{0.2})C$ high-entropy ceramic reinforced with low-loading 3D hybrid graphene–carbon nanotube. *J Adv Ceram* 2023, **12**: 341–356.
[44] Zhu ZJ, Liu YW, Qin YB, *et al.* Tough and strong bioinspired high-entropy all-ceramics with a contiguous network structure. *Nat Commun* 2025, **16**: 4587.
[45] Yang HT, Klemm S, Müller J, *et al.* Synthesis of high-entropy carbides from multi-metal polymer precursors. *J Eur Ceram Soc* 2023, **43**: 4233–4243.
[46] Hu Y, Ni DW, Chen BW, *et al.* Cf/(CrZrHfNbTa)C–SiC high-entropy ceramic matrix composites for potential multi-functional applications. *J Mater Sci Technol* 2024, **182**: 132–140.
[47] Zou HR, Zhang W, Zhang JY, *et al.* Synthesis of a novel textured high entropy M_4AlC_3 (M = Ti, V, Mo, Nb, Ta) composites with improved mechanical properties *via* spark plasma sintering. *J Eur Ceram Soc* 2024, **44**: 6889–6900.
[48] Zhai WZ, Bai LC, Zhou RH, *et al.* Recent progress on wear-resistant materials: Designs, properties, and applications. *Adv Sci* 2021, **8**: 2003739.
[49] Yin CH, Liang YL, Liang Y, *et al.* Formation of a self-lubricating layer by oxidation and solid-state amorphization of nano-lamellar microstructures during dry sliding wear tests. *Acta Mater* 2019, **166**: 208–220.
[50] Li QY, Tullis TE, Goldsby D, *et al.* Frictional ageing from interfacial bonding and the origins of rate and state friction. *Nature* 2011, **480**: 233–236.
[51] Liu DQ, Zhang HQ, You XY, *et al.* Low temperature synthesized high entropy carbide composites: A potential high temperature anti-wear material. *Ceram Int* 2024, **50**: 2111–2121.
[52] Fang Y, Zhao SQ, Li C, *et al.* Mechanical and tribological performance of (TiNbTaWMo)C high-entropy ceramics in a wide temperature range. *J Mater Res Technol* 2023, **24**: 6312–6321.
[53] Hai WX, Wu ZH, Zhang SB, *et al.* Microstructure, mechanical and tribological properties of high-entropy $(TaTiVW)C_4$ ceramics. *Int J Refract Met Hard Mater* 2023, **112**: 106114.
[54] Li JC, Zhou YC, Su YF, *et al.* Synthesis and mechanical and elevated temperature tribological properties of a novel high-entropy $(TiVNbMoW)C_{4.375}$ with carbon stoichiometry deviation. *J Adv Ceram* 2023, **12**: 242–257.
[55] Xue B, Yu HY, Huang CL, *et al.* Flexible sensors with robust wear-resistant and sensing ability: Insight on the microcrack structure, multiple interfacial bonds, and possible sensing mechanisms. *ACS Sustain Chem Eng* 2023, **11**: 7031–7041.
[56] Duan CJ, Yuan DM, Yang ZH, *et al.* High wear-resistant performance of thermosetting polyimide reinforced by graphitic carbon nitride (g-C_3N_4) under high temperature. *Compos Part A Appl Sci Manuf* 2018, **113**: 200–208.
[57] Yang JN, Li ZY, Feng XS, *et al.* Construction of a binary architecture of flower-like nickel phyllosilicate@zinc sulfide towards the robust, wear-resistant and thermal-stable epoxy nanocomposites. *Polym Degrad Stab* 2023, **207**: 110224.